Physical Biology

OPEN ACCESS

PAPER

# Guided assembly of cancer ellipsoid on suspended hydrogel microfibers estimates multi-cellular traction force

Cheng-Tai Lee[1,*], Elisabeth L Gill[2,3], Wenyu Wang[2,3], Magda Gerigk[2,3], Eugene M Terentjev[1] and Yan Yan Shery Huang[2,3,*]

[1] Cavendish Laboratory, University of Cambridge, JJ Thomson Avenue, Cambridge, CB3 0HE, United Kingdom
[2] Department of Engineering, University of Cambridge, Trumpington Street, Cambridge, CB2 1PZ, United Kingdom
[3] The Nanoscience Centre, University of Cambridge, JJ Thomson Avenue, Cambridge, CB3 0FF, United Kingdom
[*] Authors to whom any correspondence should be addressed.

**E-mail:** yysh2@cam.ac.uk and ctl40@cantab.ac.uk

**Keywords:** tissue mechanics, hydrogel, *in vitro* models, fiber force probe, helical buckling, Winkler post-buckling

**RECEIVED**
30 September 2020

**REVISED**
13 December 2020

**ACCEPTED FOR PUBLICATION**
7 January 2021

**PUBLISHED**
10 March 2021



## Abstract

Three-dimensional (3D) multi-cellular aggregates hold important applications in tissue engineering and *in vitro* biological modeling. Probing the intrinsic forces generated during the aggregation process, could open up new possibilities in advancing the discovery of tissue mechanics-based biomarkers. We use individually suspended, and tethered gelatin hydrogel microfibers to guide multicellular aggregation of brain cancer cells (glioblastoma cell line, U87), forming characteristic cancer 'ellipsoids'. Over a culture period of up to 13 days, U87 aggregates evolve from a flexible cell string with cell coverage following the relaxed and curly fiber contour; to a distinct ellipsoid-on-string morphology, where the fiber segment connecting the ellipsoid poles become taut. Fluorescence imaging revealed the fiber segment embedded within the ellipsoidal aggregate to exhibit a morphological transition analogous to filament buckling under a compressive force. By treating the multicellular aggregate as an effective elastic medium where the microfiber is embedded, we applied a filament post-buckling theory to model the fiber morphology, deducing the apparent elasticity of the cancer ellipsoid medium, as well as the collective traction force inherent in the aggregation process.

## 1. Introduction

Assembling multi-cellular aggregates in three dimensions (3D) *in vitro* is of great interests for numerous applications, ranging from drug assay development [1, 2], to fundamental investigation in tissue morphogenesis, and biofabricating tissue building blocks [3, 4]. Many types of mammalian cells can aggregate into 3D multicellular aggregates, mostly in the form of spheroids, when cultured in suspension or a non-adhesive environment [3]. With a growing focus on the roles of tissue mechanics in development and disease [5–7], a number of approaches have been developed to measure different aspects of tissue mechanics of the multi-cellular aggregates [8–16]. For instance, the effective surface tension of spheroids can be measured by instruments such as compression plate tensiometry [10, 11]. Embedding hydrogel microspheres within spheroids enabled the measurement of intra-spheroid pressure transmitted by externally applied pressures [14]. On the other hand, embedding spheroids into 3D extracellular matrices, facilitated the use of the surrounded matrix as an elastic medium to estimate the collective traction force resulting from cell-matrix remodeling [16]. Despite these progresses, there have been limited approaches to evaluate the collective traction forces generated during the self-assembly process of multicellular aggregation. To achieve this, the measurement framework should allow the freedom of cell–cell interaction (thus minimizing cell–probe interaction), while simultaneously allowing to probe the traction forces locally, and in an *in situ* and non-destructive manner.

Here using hydrogel microfibers as a minimalistic guide for multi-cellular aggregation, we generate cancer ellipsoid-on-strings around individually suspended microfibers, giving the potential of adapting such a guided assembly scheme to probe the aggregation tissue mechanics. Individually suspended microfibers of chemically crosslinked gelatin, tethered over a distance of 3 mm, were fabricated by

3D low-voltage electrospinning patterning (3D-LEP) [17]. When submerged in the culture media, the fibers swell by about 50% so that their length increases by ∼15% [18]. Young's modulus of swollen crosslinked gelatin fibers was previously found to be in the order of 100 kPa [19], which is a typical value of a rubber modulus, and also close to the modulus of pre-calcified bone [20]. The radius of these soaked hydrogel microfibers is 1.5 to 5 $\mu$m [18, 19], in a range similar to certain anatomical features of the brain, such as the white matter tracks and brain microvasculature. With this in view, we used U87, a brain cancer (glioblastoma) cell line, as a model system to form aggregates around individually-suspended gelatin microfibers. Over the course of cell culture, the multi-cellular aggregates developed into characteristic cancer ellipsoid-on-string guided by the fibers; at the same time, we found that fiber conformation was simultaneously changed due to the localized collective traction forces. We discovered interesting and unusual phenomena of fiber straightening, simultaneously with distinct fiber-buckling in the core of these ellipsoids. Since the dimensions and the mechanical properties of elastic fibers are known, we explored the possibility of using the microfiber conformation as an *in situ* force probe to estimate the cancer aggregate mechanics, by comparing with a theoretical model based on 3D fiber buckling in an elastic medium.

The mechanics of an elastic filament subjected to a compressive force (traction) along its axis has a long history. Classical Euler buckling (1757) describes the threshold instability when a free-standing filament (simply-supported at both ends) is compressed [21–25], giving the celebrated expression for the critical buckling force: $P_{\rm cr}^{\rm E} = \pi^2 B/L^2$, where $B$ is the filament bending rigidity, and $L$ is the total filament length. The bending rigidity $B$ in experiments can be estimated by the expression $B = YI$, where $Y$ is Young's modulus of the filament, while $I$ is the second moment of the cross-section area and is related to its geometric shape. For a round cross-section of radius $R$, the second moment equals to $\pi R^4/4$, thus giving $B = \pi Y R^4/4$. From Euler's expression, a longer filament is easier to lose mechanical stability and buckle under compression. The buckling shape at this critical point is sinusoidal, with the critical wavelength being: $\lambda_{\rm cr}^{\rm E} = 2L$. The post-buckling shape of the free filament (called the 'elastica theory') has been originally studied by Euler and Bernoulli, and later generalized by Cosserat (1907) [26].

When a filament under compression is embedded in an elastic medium, its buckling instability is different. The Winkler theory (1867) was originally developed for rods embedded in soil [21, 27], but later had a profound influence on adhesion and soft matter applications [28–30]. The lateral deflection of the filament is restricted, and the Winkler model (with the filament ends both simply-supported) predicts the critical buckling force $P_{\rm cr}^{\rm W}$ and the wavelength of the sinusoidal shape $\lambda_{\rm cr}^{\rm W}$: $P_{\rm cr}^{\rm W} = 2\sqrt{Bk}$ and $\lambda_{\rm cr}^{\rm W} = 2\pi\left(B/k\right)^{1/4}$, where $k$ is Young's modulus of the elastic medium, and $B$ is the filament bending rigidity, the same as defined in Euler's model. Unlike in Euler buckling, the Winkler results for a sufficiently long filament ($L > \lambda_{\rm cr}^{\rm W}$) do not depend on the total filament length $L$, but have an intrinsic length scale. Of course, there would be a crossover to Euler results of a single half-wavelength buckling when $L < \lambda_{\rm cr}^{\rm W}$.

It turns out that in the post-buckling regime, the shape of the elastically constrained filament does not have to remain flat: recently Chen and Chen have developed a model describing the 3D version of Winkler's problem, with the filament adopting a helical shape [31, 32]. In this paper, we find that our microfibers buckling inside the developed cancer ellipsoids are following such a helical morphology, which will be the base of our analysis.

## 2. Materials and methods

### 2.1. Suspended fiber device

Suspended fiber devices were composed of fibers drawn from a gelatin (Porcine, type A, Sigma Aldrich, G2500) solution across 3D printed supports (Ultimaker PLA filament) using a pre-established method [17]. Devices were designed in Autodesk Inventor (Autodesk Inc., USA), 3D models were 'sliced' as GCode files and optimised for efficient and throughput production in Simplify 3D® (Simplify 3D, USA). Devices were designed with fibers suspended 1.2 mm above the buildplate, spanning across 3 mm at an inter-fiber pitch of approximately 200 $\mu$m, and the overall device height was 1.5 mm.

### 2.2. Solution preparation

Gelatin solution was prepared as previously described in the weight ratio 19:33:22:26 gelatin: acetic acid: ethyl acetate: deionized water [19], with 6 v/v% glyoxal (40% in $H_2O$, Sigma-Aldrich, 128465) added prior to printing as a cross-linking agent to stabilise fibers in cell media. Glyoxal was mixed into the gelatin solution with a magnetic stirrer for 30–40 minutes, the solution was left to stand for 5 minutes to allow bubbles to rise to the surface, before loading into a 1 ml syringe and starting a print.

### 2.3. Device fabrication and preparation for cell culture

The flowrate of electrospinning solution was controlled with the Elveflow pressure controller (OB1 MK3, Elveflow, France) in the range of 30–200 mBar pressure. Solution was spun with applied voltage of 130 V. LEP print-head translation was 7500 mm min$^{-1}$, print-bed temperature was 70° C to assist PLA adhesion and solvent evaporation from

patterned fibers. PLA was printed at 190° C with optimized retraction settings for each print file. A print file which assembled a batch of 8 devices had a run time of ∼12 minutes. Devices were printed on 24 mm × 50 mm glass cover slips to provide stable PLA adhesion to the build plate during printing and for ease of handling post-printing. Devices were stored in covered containers for 24 hours at room temperature to ensure complete solvent evaporation. Next, devices were transferred from the glass coverslips to 12-well tissue culture plates before sterilization under a UV lamp for 20 minutes (ESCO UV-30A, 253.7 nm predominant wavelength) and soaked in cell media overnight before cell seeding.

### 2.4. U87 cell culture on suspended fiber devices

Human glioblastoma cells U-87 cell lines were purchased from ATCC (HTB-14). Cell culture media consisted of 10 v/v% fetal bovine serum (Sigma-Aldrich, F0804) in 500 ml of Dulbecco's Modified Eagle Medium (DMEM, Sigma-Aldrich D6429). U87 cells were cultured to confluence in a T75 flask and passaged following standardized protocols with trypsin EDTA. Following centrifugation at 1000 rpm for 5 minutes the supernatant was thoroughly removed and a fixed volume micro-dispenser (Drummond Scientific, 41121505) was used to seed 1 $\mu$l of cell pellet on a suspended fiber device immersed in cell media. Cell media was replenished every 2 days and cells were cultured under incubation conditions of 37°C, 5% $CO_2$ for 13 days in total.

### 2.5. Live/dead staining

Live/dead viability/cytotoxicity assays (ThermoFisher Scientific, L3224) were performed on the samples following manufacturer's protocol on a Day 10 culture and imaged with a Zeiss Axio Observer Z1 fluorescence microscope.

### 2.6. Immunostaining and imaging

Cells were fixed in 4% paraformaldehyde (PFA, Sigma-Aldrich) and permeabilized with 0.2% Triton 100X (Sigma-Aldrich) in phosphate buffered saline. Non-specific antibody interactions were blocked by incubating the cells with 4% albumin from bovine serum (BSA, Sigma-Aldrich, A7906) in PBS for 1 hr. For nuclear and cytoskeleton staining, eBioscience™ CyTRAK Orange™ (Invitrogen, 65-0881-92) and GFAP Monoclonal Antibody (GA5), Alexa Fluor 488, eBioscience™ (Life Technologies, 53-9892-82) were respectively used at 1:1000 dilutions in PBS. The devices were washed and then stored in PBS at 4°C and fluorescence imaging was performed within 8 days from staining. Subsequently, fluorescent images were acquired by Leica SP5 confocal microscope using a 10x objective. Z-stacks were captured over a depth of 151.16 $\mu$m with a 2.52 $\mu$m step size. Three-dimensional reconstruction of the confocal image slices was performed with Fiji ImageJ.

### 2.7. Ethics

Ethics approval is not required.

## 3. Results and discussion

### 3.1. Guided assembly of cancer ellipsoids-on-strings on gelatin fibers

Suspended crosslinked gelatin microfibers of a variety of patterns, tethered to 3D printed thermoplastic supports, can be designed and fabricated using 3D-LEP [17]. Whilst the microfibers are patterned as straight dry spanning structures with a fixed length, as they are a hydrogel, they swell in culture media and become relaxed and free-floating as a result of solution uptake, schematically shown in figure 1(A).

Tethering the hydrogel microfibers to a rigid thermoplastic structure preserves the structural integrity of the entire fiber device, for cell culture and subsequent immunofluorescence staining. As gelatin has inherent Arg-Gly-Asp (RGD) sequences which provide sites of cell attachment, U87 cells spontaneously adhere and cumulate around the fibers upon seeding, without the need for additional coating of attachment factors, schematically shown in figure 1(B). As illustrated by the bright-field microscopic images over the duration of the culture in figure 1(C), cancer cells populated along the entire fiber length, initially following the relaxed, curly fiber contour forming cancer cell-strings (at ∼30 hrs). At around day 3, aggregation starts on individual fibers at select segments along the fiber length. Gradually, distinct cancer 'ellipsoid-on-strings' are developed (seen at day 9), evidently centered around fiber. During cellular growth and aggregation, the overall conformation of an individually suspended microfiber evolves, seemingly following the mechanical behavior of the attached cells.

Figure 2 shows immunofluorescence images of the day 13 multicellular assembly, forming ellipsoid-on-strings along the entire spanning distance of the suspended gelatin microfibers. We see two distinct regimes of coexisting filament morphology, determined by the cellular aggregation. In the region where adherent cells form a coating of a few cells thick, these cells elongate and align along the fiber, while the fiber itself is straight and taut, as seen in the bright-field microscopic images in figure 2(B), all its original length slack being taken away by the buckled region. In other words, the overall contour length of the microfiber is roughly conserved during the culture period, and the reduction in the apparent length in the tensed fiber segment is converted into length consumed by the crumpled fiber segment embedded within the ellipsoid. Where the large aggregates consolidate, the spheroidal shapes normally formed by U87 aggregates in suspension culture, are now guided by the fiber and elongated along the fiber axis into ellipsoidal shapes. The fiber segment lying within

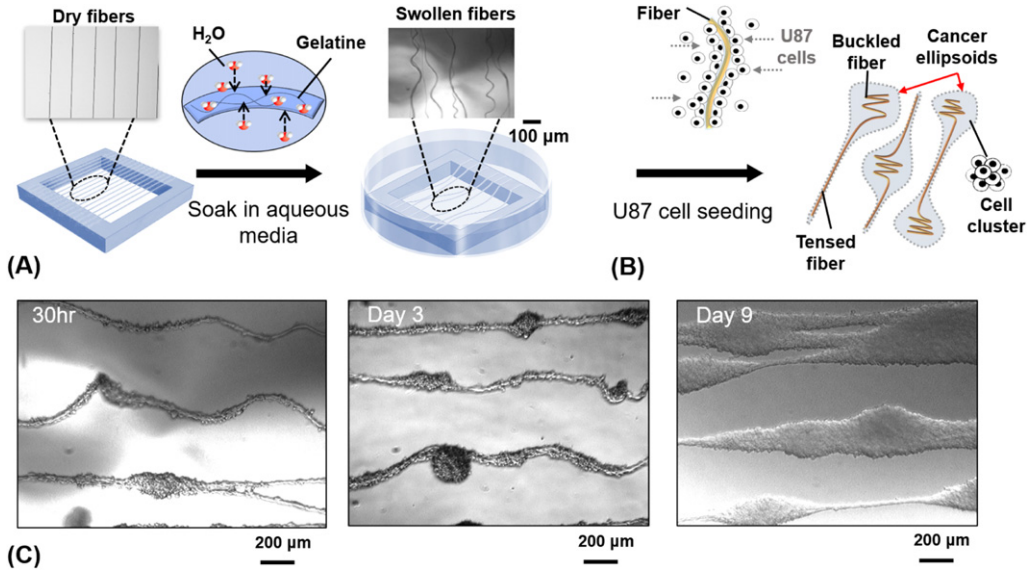


**Figure 1.** (A) Scheme illustrating the tethered, suspended gelatin microfiber device produced by 3D-LEP, with insets showing the as-produced straight dry fibers, and the post-soaking swollen fibers with their length increased by approx. 15% (estimated by comparing the projected fiber contour length before and after soaking). (B) A carton overview of the process of cell seeding and cell aggregation on the gelatin microfibers. (C) Bright-field images of the evolving cell-fiber interaction captured at different culture time points.

such an ellipsoid adopts a characteristic 'crumpled' shape, which could be a consequence of its buckling under compression force. Such an effect has not been reported before. The core of the dense cellular cluster seemingly exhibits a necrotic center, as shown by live/dead staining in figure 3. Thus the live cells at the periphery of the ellipsoid is expected to provide the majority of the traction force on the gelatin segment inside. Therefore, we postulate that when the elastic fiber is embedded inside such an ellipsoid, its two ends (where the fiber crosses the shell) experience a significant compressive force, while the inside section of this fiber experiences little external forces generated from neighboring cells. Instead, these cells in the core of the ellipsoid only act as a weak elastic resistance for the embedded fiber segment. Evidence further supporting this postulation is shown in the immunofluorescence image of the mid-plane of fiber-cell aggregate in figure 2(A). The fluorescence signal of GFAP (a protein indicated in astrocytes' cytoskeleton and mechanical strength [33–37]), appears as a thin shell at the ellipsoid peripheral, but is largely absent at the aggregate's center. In fact, the combination of the 'strong' external shell and the 'soft' interior of spheroid cell aggregates was also reported in a recent experiment of measuring the shape relaxation time, when applying compression to squeeze a spheroid aggregate into a barrel-like morphology between two plates, and then releasing it [38].

It is of interest to determine the number of cells aggregated in the cancer ellipsoids. As the ellipsoid is too thick to easily obtain fluorescence imaging of its entire 3D volume, we look at the cellular assembly at the straight segment of the microfiber to give an indication on the density of cells. By counting the number of cells (i.e. nuclei) present within a clearly imaged volume around the fiber, e.g. figure 2(B), the density of the cells aggregated there is estimated to be $\sim$1/3600 $\mu m^{-3}$. With the volume of the Day 10–13 mature ellipsoid aggregate between $2–4 \times 10^7$ $\mu m^3$, a conceptual of the total number of cells within one ellipsoid aggregate is estimated to be 5000 to 10 000. However, beware that the cell density around the shell of an ellipsoid is expected to be higher than 1/3600 $\mu m^{-3}$, since the cells not in contact with the fiber are able to compress. On the other hand, the middle of the consolidated aggregate contains a high fraction of dead or dying cells (as their nutrition is restricted), thus giving a lower density of cells. Because the thin shell apparently occupies much less volume than the necrotic interior of the cell aggregates, overall, the estimated range of the number of cells inside one ellipsoid aggregate above is likely an over-estimate (i.e. forming an upper-bound for this number).

All in all, we find a dramatic effect of the fiber buckling inside the ellipsoid aggregates seen in figure 2(A), which we postulate to act as an elastic support for the fiber segments embedded inside, and provide compression through the thin shell of living cells at their ellipsoid periphery. The analysis of this phenomenon is the main subject of this paper.

### 3.2. Helical buckling in an elastic medium with compression

Since the dimensions and the mechanical characteristics of the crosslinked gelatin microfibers are established, and may be assumed constant during the

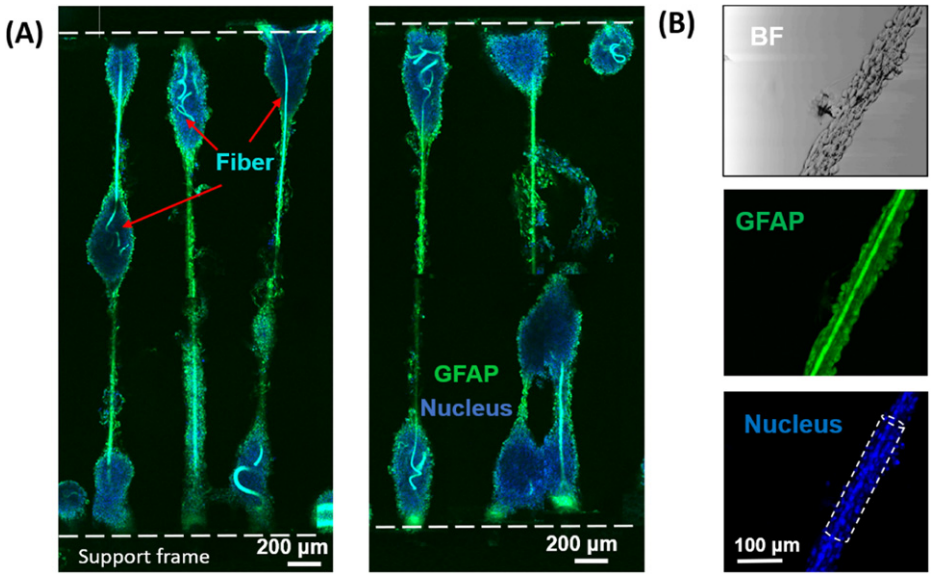


**Figure 2.** (A) Immunofluorescence images of ellipsoid-on-string formed along the entire spanning distance of the suspended gelatin microfibers. The crumpled fiber inside the ellipsoidal aggregates has non-specific binding to both staining reagents, and is clearly visible inside the cluster. Note that the GFAP staining is concentrated in the thin shell surrounding the cancer ellipsoid. Dotted lines are used to indicate the regions of the support frame. (B) Bright field (BF) and immunofluorescence images showing multi-cellular clustering forming a rod-shape at the straight fiber segment at day 13.

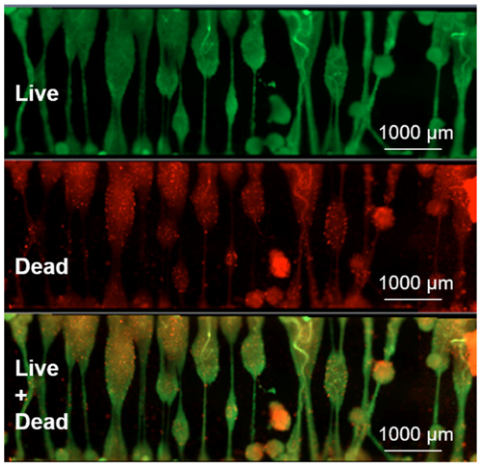


**Figure 3.** Live/dead staining images showing the ellipsoid-on-string (day 10) formed on the entire microfiber-device. The channels showing the live and dead cells are combined in the last image. It is clear that the dead cells are prevalent inside the aggregates; the residual weak red fluorescence on the straight fiber segments is due to the non-specific fluorescence signal of the gelatin.

culture period, we explore the possibility of using these fibers as an *in situ* force probe to estimate the cancer aggregate mechanics, by exploring the filament buckling mechanics. We focus on an individual ellipsoid compressing the filament that threads through it, ignoring the possible weak fiber pre-tension due to other ellipsoids: the fibers initially are in a loose state, and only straighten as ellipsoids are growing.

From fluorescence images in figures 2 and 3, the projected length of the gelatin fiber inside the cancer ellipsoid is ∼500 $\mu$m along the original fiber axis. The fiber shape therein resembles a helix with 4 to 6 turns, with a slight localization effect (i.e. the helix radius gradually decreases along the fiber axis), while the remaining part of the fiber outside the ellipsoid aggregate remains straight, see figures 1(B) and 2(A). The aggregate interior is treated as an 'apparent elastic medium', with the gelatin fiber subjected to a pure compressive load from the contractile outer shell of this cancer ellipsoid, as described in the previous section. This characteristic buckled shape allows the use of the ideas of Chen on the helical buckling of a filament in an elastic suspending medium [32].

Figure 4 shows the scheme of the Chen model of helical buckling morphology, making a parallel with our observation. Under the assumptions that no sliding occurs at the interface between the medium and the fiber surface, and that a constant compression force/strain propagates throughout the whole fiber axis (i.e. ignoring the shear stress from the medium acting on the fiber to lessen the force propagated), Chen *et al* derived approximate analytical relations of the helix pitch size (periodicity) $\lambda$ and radius $\rho$ for a volume-conserved fiber and elastic medium (i.e. Poisson ration = 0.5), as functions of the compression strain $\varepsilon_{\mathrm{com}}$ of the medium in the post-buckling regime [32]:

$$\lambda = \lambda_{\mathrm{cr}}^{\mathrm{W}}\,(1-\varepsilon_{\mathrm{com}})\,;\quad \rho = \frac{1.276}{2\pi}\,\lambda_{\mathrm{cr}}^{\mathrm{W}}\sqrt{\varepsilon_{\mathrm{com}}-\varepsilon_{\mathrm{cr}}^{\mathrm{W}}}, \tag{1}$$

where $\lambda_{\mathrm{cr}}^{\mathrm{W}}$ is the periodicity at the buckling threshold. In Chen's paper this is denoted as the initial $h$, and we note that the numerical factor 6.160 in its definition is almost identical to the numerical factor of $2\pi$ given in the Winkler model. Thus, we replaced the original

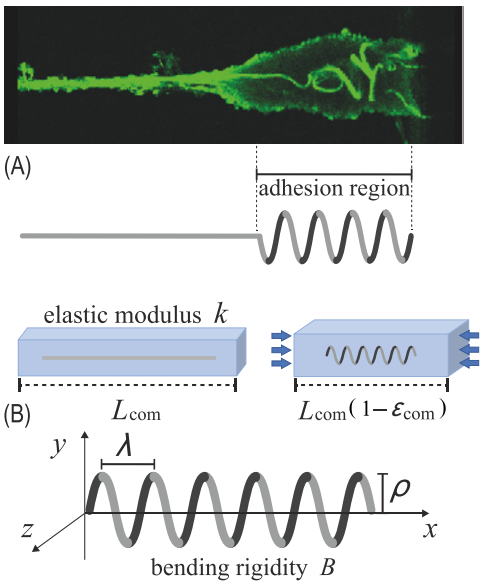


**Figure 4.** (A) Fluorescence image of the microfiber with cell aggregate, simplified into a cartoon of helical buckling in the adhesion region. (B) Schematic helical buckling shape and parameters in Chen's model [32]. $L_{com}$ here is the length of the embedding medium before deformation, and will later be compressed and shrink to $L_{com}(1-\varepsilon_{com})$. The helical buckling pattern has the pitch size $\lambda$ and the radius $\rho$.

factor with $2\pi$ to recover the 2D Winkler model at the critical buckling point: although this connection was not specifically pointed in Chen's paper, from a physical point, the radius of the helix has to evolve from zero at critical buckling point. At this point $\rho = 0$, the in-plane 2D Winkler model and the Chen's 3D helix model are strictly equivalent. That is, the critical buckling periodicity $\lambda_{cr}^{W} = 2\pi(B/k)^{1/4}$, and the critical buckling strain of the embedded filament $\varepsilon_{cr}^{W} = P_{cr}^{W}/YA = 2\sqrt{Bk}/YA$ (or equivalently, the strain of the elastic medium at this point of filament critical buckling). $k$ is Young's modulus of the medium, while $B$, $Y$ and $A$ are the bending rigidity, Young's modulus and the cross-section area of the fiber, respectively.

Considering that the more natural quantity to use and compare in this cell-fiber buckling system is the collective traction force generated by U87 cells, the compression strain $\varepsilon_{com}$ of the medium needs to be transformed into the compressive force $P$ upon the fiber segment ends, to allow further application of these formulas to our helical buckling problem. Before/At critical buckling point, the strain $\epsilon_{com}$ of the elastic medium equals to the axial strain $\epsilon_{m}$ of the embedded fiber. Yet, after fiber buckling into a helix, not all the strain from the elastic medium will be converted into the fiber axial strain $\epsilon_{m}$. Under the assumption of no sliding at the interface between the filament and the medium, and the absence of shear stress from the medium acting on the filament (i.e. a constant filament axial strain along the filament axis), this relation is described in equation (5) of Chen's model [31] as:

$$\frac{2\pi^2\rho^2}{\lambda^2} + \varepsilon_m = \varepsilon_{com}, \quad \text{for } \varepsilon_{com} \geqslant \varepsilon_{cr}. \tag{2}$$

Combining the helix expression in the post-buckling regime of (1) and the strain conversion of (2) results in a cubic equation for $c\varepsilon_{com}$, which then can be solved to find the strain-force transformation after the buckling point. However, this exact solving a cubic equation is cumbersome, and will not help developing a clear physical understanding. For our purpose of elucidating the order of the magnitude of the compression force (since in experiments we already have a large uncertainty in shape and mechanical parameters), it may be sufficient to simply assume $(1-\varepsilon_{com}) \sim 1$ for a neat $\varepsilon_{com}$-expression for later qualitative analysis:

$$\varepsilon_{com} = \frac{P - 0.814P_{cr}^{W}}{0.186YA}, \quad \text{for } \varepsilon_{com} \geqslant \varepsilon_{cr}. \tag{3}$$

Here $P$ is the compressive force acting on the ends of the fiber, while $P_{cr}^{W} = 2\sqrt{Bk}$ is the Winkler's critical buckling force. At $\varepsilon_{com} = \varepsilon_{cr}$, we recover $P = P_{cr}^{W}$ as expected. Inserting this transformation of (3) into (1), we arrive at our final expressions of $\lambda$ and $\rho$ for the analysis of our experiments:

$$\begin{aligned} \lambda &= \lambda_{cr}^{W}\left(1 - \frac{P - 0.814P_{cr}^{W}}{0.186\ YA}\right); \\ \rho &= \frac{1.276}{2\pi}\ \lambda_{cr}^{W}\sqrt{\frac{P - P_{cr}^{W}}{0.186\ YA}}, \end{aligned} \tag{4}$$

where $\lambda_{cr}^{W}$ and $P_{cr}^{W}$ are the Winkler parameters, given below (1), both of which depend on Young's modulus $k$ of the medium, and fiber bending rigidity $B = \pi YR^4/4$, for a fiber with a round cross-section of radius $R$ and Young's modulus $Y$. The cross-section area $A$ equals to $\pi R^2$ for a solid cylindrical fiber.

To elucidate the magnitude of the force the ellipsoidal aggregate produces in this post-buckling regime, it is necessary to know the elasticity of the aggregate interior (the parameter $k$ in the Winkler and Chen theory). We assume its Young's modulus is quite low, given the noticeable fraction of dead or dying cells in this interior, yet this elastic modulus has to be used as an unknown fitting parameter to be determined. The helix pitch size $\lambda$ and an estimate of the helix radius $\rho$ in the buckling pattern are extracted from the fluorescence images, while the fiber parameters $Y$ and $A$ (or the fiber radius $R$) are measurable at the preparation stage of our experiments. The two quantities left to determine here are Young's modulus $k$ of the medium (ellipsoidal cell aggregate itself) and the compressive force $P$ generated by this aggregate.

### 3.3. Traction force and elasticity of the ellipsoidal cell aggregates

The helices in the experiment images show 4 to 6 full turns within the projected length of ~500 $\mu$m along the $x$-axis, giving the helix pitch size $\lambda$ from 125 to 80

$\mu$m. The helix radius $\rho$ varies between 5 and 40 $\mu$m. We take the modulus of a swollen gelatin fiber $Y = 100$ kPa, while the radius $R$ of the fiber in experiment is observed to sit between 1.5 and 5 $\mu$m, resulting in range of values of the bending rigidity (through $B = \pi YR^4/4$). With these experimental values of $\rho$, $\lambda$, $Y$ and $R$, (4) can be used to obtain the elastic modulus $k$ of the cell aggregate and the compression force $P$. However, the values of $\rho$ and $\lambda$ in experiment cover a certain range, which would, in turn, estimate quite a broad range of $k$- and $P$-values. We decided to first use (4) and plot the numerically-solved $k$-value against $\lambda$ within the experiment range between 80 and 125 $\mu$m, while at several values of the helix radius $\rho$ and with three different sizes of fiber radius $R$. This way, the magnitude of the $k$-value in our experiment can be captured, allowing the further determination on which values of $k$ and $R$ should be adopted to estimate the compressive force $P$, and to re-calculate the helix radius $\rho$ in matching with experiment. In the following analysis, we all constrain the pitch size $\lambda$ between 80 and 125 $\mu$m.

Figure 5 shows that as the helix radius $\rho$ increases from 10 to 40 $\mu$m, the estimated elastic modulus $k$ of the interior of cell aggregate dramatically decreases from a few hundreds of Pa to below 50 Pa, while a thinner fiber predicts a weaker elasticity $k$ at each $\rho$-value. Further increase in $\rho$ beyond 40 $\mu$m will cause an even smaller $k$-value, which may not be reasonable: Young's modulus of tissue can vary significantly depending on the type of tissue in measurement, starting from 100 Pa (brain) to 5 kPa (skin), to 10–30 kPa (muscles) [39–43]. Without doubt, our cell aggregate is not a 'proper' tissue as its interior has a high proportion of dead and dying cells, not to say the cell population is almost homogeneous and entirely made up of cancer cells. So the 'safe' strategy here is to let this $k$-value range from 50 Pa to a few hundreds of Pa in later investigation of the compressive force $P$.

Since $k$ is now constrained, fibers with radius $R = 2.5$ $\mu$m can only produce the small helix radii in experiment (only when $\rho$ is below 10 $\mu$m, $k$ can still be larger than 50 Pa in this case). To further produce larger $\rho$-values in this case requires an even smaller $k$-value, falling out of the reasonable range we discussed above. As for the case $R = 3.5$ $\mu$m, the resultant helical patterns can at most have $\rho \leqslant 20$ $\mu$m within the $k$-range we take. Therefore, $R$ has to be at least 5 $\mu$m or even larger (thicker fibers, may be produced due to different individual extent of solution uptake during swelling) to reach $\rho \geqslant 30$ $\mu$m, while not requiring an unreasonably weak interior elasticity $k$. On the other side, for fibers of a large $R$ to have smaller $\rho$-values, it can easily be achieved by increasing the elasticity $k$. Therefore, to cover the wide range of $\rho$- and $\lambda$-values we see in experiment, it has to be $R \geqslant 5$ $\mu$m, while $k \geqslant 50$ Pa. Note that the Young's modulus of a fiber enters our theory in combination with $R$, (as $YR^2$ or as $YR^4$ in bending rigidity $B$), so the sensitivity to changing $R$ shown in figure 5(A) could be directly mapped to $Y$.

We take $R = 5$ $\mu$m as an example, and plot $\lambda$ and $\rho$ against the compression force $P$, at $k = 50$, 100 and 200 Pa. By confining $\lambda$ between 80 and 125 $\mu$m as before, we find the corresponding window for $P$ shown in figure 5(B). Subsequently in figure 5(C), we use this $P$-window to estimate the range of $\rho$. Combining these two plots, the $P$-window obtained in this procedure is of the range from 0.3 to 1 $\mu$N. The higher force corresponds to a weaker elastic modulus $k$ and a wider helix radius $\rho$.

Note that $\rho$ in our experiment can be up to 40 $\mu$m, which further requires a larger fiber radius (a more rigid fiber as it will become) to match the pitch size $\lambda$ seen in our experiment. This, in turn, predicts a stronger compression force $P$ exceeding 1 $\mu$N, which can be checked from the $\lambda$-expression in (4)—a more rigid fiber will have a longer $\lambda_{cr}^{W}$ at the critical buckling point; therefore to shrink into a fixed $\lambda$-value, $P$ must be further increased. This magnitude of $P$ in the $\mu$N regime is not unreasonable. Cell traction force of one single isolated cells varies from a few to tens of nN [44–46]. In particular, one single U87 cancer cell has been reported to generate a traction force of 50 nN [11]. Using this value, to generate 1 $\mu$N requires 20 U87 cells. Our ellipsoid aggregate contains 5000–10 000 cells (though it is an over-estimate, as given in section 3.1), and should be able to produce the buckling force required in our experiment, considering the large difference in these two numbers of cells (thousands vs tens).

### 3.4. Theoretical validation

A rough estimate for the value of the compressive force applied on the internal fiber segment may be deduced, by finding the tensile force acting on the contact area of the fiber with the thin shell of the living cells of the ellipsoid aggregate. We define the thickness of the thin shell of the cell aggregate as $h$, and the contact angle of this shell with the fiber segment end (at the periphery of the cell aggregate) is $\theta$. Theses two shape parameters $\theta$ and $h$ cannot be measured precisely in our experiment, yet to serve the purpose to justify the order of the magnitude of the force we estimated via the helical buckling model, an approximate conceptual value would be sufficient. The total pulling force from this shell (i.e. a net compression upon the ends of the fiber segment inside the cell aggregate) can be calculated though: $2\pi RT\cos\theta$, where $R$ is the fiber radius as defined before, $T$ is the surface tension of the cell aggregate, $\cos\theta$ denotes the fraction of the tensile force by the shell acting as compression along the straight fiber axis. The total surface tensile force $2\pi RT$ may be derived from the active stress $\sigma$ of myosin proteins acting on the area $A$ of the cortical layers inside cells, using the relation $2\pi RT = \sigma A$.

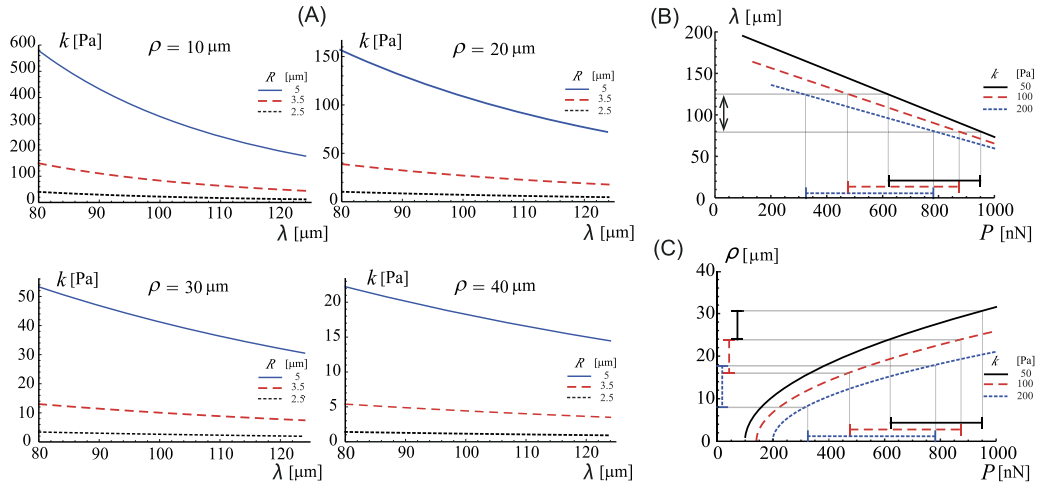


**Figure 5.** (A) The elastic modulus $k$ of the cell aggregate, plotted against the helix buckling pitch size $\lambda$ within the experiment range (from 80 to 125 $\mu$m), with the helix radius $\rho = 10$, 20, 30 and 40 $\mu$m. In each plot, the radius of the fiber $R = 5$, 3.5 and 2.5 $\mu$m (blue solid, red dashed and black dotted; from top to bottom, respectively). (B) The helix pitch size $\lambda$ and (C) the helix radius $\rho$, plotted against compression $P$ using (4), at $k = 50$ (black, solid), 100 (red, dashed) and 200 (blue, dotted) Pa, with the fiber radius $R = 5$ $\mu$m and Young's modulus of the fiber $Y = 100$ kPa. In (B), these three linear curves start from their own critical buckling forces. The colored bars show the range of $P$ obtained by inserting $\lambda$-values within the experiment range between 80 and 125 $\mu$m (confined by horizontal gray lines), at each $k$-value (same matching of colors and styles). In (C), these derived experiment ranges of $P$ (bars above $P$-axis) are then used to find the corresponding ranges of $\rho$-values (bars along the $\rho$-axis), with same style-matching.

The area $A$ of cortical layers is assumed to equal to the contact area of the shell surrounding this fiber segment: $A = 2\pi Rh$. Undoubtedly, this assumption may over-estimate the real thickness of cortical layers, which do not fully occupy the entire internal of cells. Therefore, the total tensile force estimated later using this $A$-expression is likely to be an upper bound of the compressive collective force from the cell aggregate. In our example, $R = 5$ $\mu$m, while we take the rough estimate $\theta = 30^\circ$ from the images of the ellipsoids in figure 2, giving $\cos\theta \sim 0.86$. The shell thickness $h$ may be approximately the same as, or a bit larger than, the thickness of the cells coated onto the straight fiber part outside the ellipsoids in figure 2(B), based on the observation that living cells aggregated onto the straight fiber part seemingly showed the same thickness of fluorescence signal by GFAP staining as at the periphery of the ellipsoid, thus taking $h \sim 50$ $\mu$m (which corresponds to a layer of 3–5 cells in the BF image there). The data for the active stress $\sigma$ of U87 cells is absent, but as a conceptual estimate, we may use the value given in Tinevez's work of mouse L929 fibroblasts $\sigma = 2400$ Pa [47], which can also exhibit a high contractility, thus possibly approaching the active stress value for highly contractile U87 cells in our case. Altogether with these parameter values, the net compressive force acting on the fiber segment ends is calculated via: $2\pi Rh\sigma\cos\theta = 2\pi \times 5 \cdot 10^{-6} \times 50 \times 10^{-6} \times 2400 \times 0.86 \sim 3.24 \times 10^{-6}$ N. This force value is in the regime of $\mu$N, where our estimated force can fall into when a larger helix radius than 30 $\mu$m is observed, and is expected to be the upper bound for the compressive force our cell aggregates can generate.

Another way to estimate this compressive force is to count the number of living cells of the ellipsoidal shell that are in contact with the fiber segment. We earlier took the shell thickness to be of 3–5 cells with $h = 50$ $\mu$m, implying the thickness of one cell is 17, 12.5, and 10 $\mu$m (estimated using the shell thickness of 3, 4 and 5 cells, respectively). The range of the total number of cells of the shell in contact with the fiber is then: from $3 \times (2\pi R/17)$ to $5 \times (2\pi R/10)$, giving 6–16 cells with $R = 5$ $\mu$m. Using the traction force of 50 nN measured with a single U87 cell given in [16] and the contact angle $\theta$ of 30°, the range of the net compressive force is approximately 260–690 nN, covering partially the range of the windows shown in figures 5(B) and (C). Although these two estimates are very crude (by surface tension estimated through active stress from myosin proteins, and the counting of the number of living cells onto the fiber in the aggregate shell), they are comparable to the magnitude of our estimated force. This shows the possibility to use this system of fiber-crumpling in cell aggregates as a potential force probe, with the application of the helical buckling theory. To obtain a more accurate estimate of collective contraction force from cell aggregates, undoubtedly, further advanced development of the helical buckling theory (e.g. using a buckling shape with a decaying length, closer to the experimental images) and elucidation in some other experimental parameters, such as elasticity of the interior of cell aggregates, are required.

On the other hand, if tensile forces are really present in external filament segments, the buckling force on the internal fiber segments (inside ellipsoids) then becomes the difference between the traction force of the ellipsoid and the overall weak tensile force. The analysis of all the ellipsoids along the same fiber and their anchored positions on the fiber would then be necessary.

## 4. Conclusion remarks

There have been limited approaches to evaluate the collective traction forces generated during the self-assembly process of multi-cellular aggregation. Our measurement framework of ellipsoids-on-strings minimizes cell–probe interaction, by maximizing the freedom of cell–cell interaction, and simultaneously allows to probe the cell traction forces locally in an *in situ* and non-destructive manner. These features of our experiment framework make a stark contrast with previous force-probe systems that have to either constrain spheroid cell aggregates into 3D extracellular matrices (interfering with cell–cell interaction) [16], or embed hydrogel microspheres inside the targeted spheroid cell aggregate (which does not probe the active forces generated by the cellular aggregate).

In particular, the dimension of the cross-linked gelatin fiber between 1.5 and 5 $\mu$m in radius is crucial to achieve these unique characteristics: if the fiber radius is too small, cells in suspension will not easily spread and adhere onto the narrow fiber surface; while if too thick, a large fiber probe, compared with the few layers of cells in aggregate thickness, may potentially interfere with cell–cell interaction and cell aggregation. To mitigate this reciprocal effect between the fiber thickness and cell aggregates, a small volume occupied by fiber segments within these aggregates is anticipated. Moreover, this particular range of the fiber radius, in fact, depends on the choice of the fiber material, which has to provide a suitable bending rigidity in order to produce a readily-perceivable buckling pattern, when subjected to compressive forces ranging between a few hundreds of pN and 1 $\mu$N from U87 cell aggregates. In making fibers, the use of crosslinked gelatin, typical in the order of 100 kPa in Young's modulus, may consequently be unique and well-suited for investigating the U87 aggregate system (or other cell aggregate systems with a similar range of cell traction forces), which we shall discuss.

In our experiment, the crosslinked gelatin fiber of radius $R = 5\ \mu$m, with the projected length of the fiber segment around 500 $\mu$m, the minimum helix pitch size of 80 $\mu$m and the maximum helix radius of 40 $\mu$m (to estimate the maximal volume of the fiber segment), would occupy $1.3 \times 10^5\ \mu\text{m}^3$ (~0.43 v/v% of the ellipsoid cell aggregate)—giving an almost negligible occupation ratio. However, if a softer material is used to replace crosslinked gelatin, for example, with Young's modulus of 1 kPa (representation of lightly cross-linked hydrogels), the fiber radius would become ~28 $\mu$m, in order to achieve the same bending rigidity and thus the same pronounced helical buckling pattern, and would occupy ~14 v/v% of the cell aggregate. This dramatic increase in the volume occupation of fibers inside cell aggregates would increase the risk of cell–probe interference. In contrast, although a larger Young's modulus of the material is preferred (to have a smaller fiber radius and lessen this reciprocal effect between cells and the fiber probe), U87 cells in suspension will not easily adhere onto fibers of small size, hence forming an upper-limit for Young's modulus of fiber material. Consider a fiber of extreme rigidity $Y = 1$ GPa (typical of thermoplastics), subjected to a typical force around 1 $\mu$N produced by cell aggregates and the elasticity $k = 50$ Pa of the interior of these aggregates in the fiber-crumpling system. With the minimum radius $R = 1.5\ \mu$m required for cell attachment onto the fiber surface, a much smaller helix radius $\rho \sim 1\ \mu$m is obtained from (4). The resultant small helix radius is of the same magnitude of the fiber radius in this case, which makes it difficult to measure and perceive from fluorescence images.

In this paper, we discover an unusual phenomenon of fiber straightening, simultaneously with distinct fiber-buckling in the core of cell aggregate ellipsoids. We explore the possibility of extracting the net compressive force this cell aggregate generates onto the fiber segment ends (at the poles of these ellipsoid aggregate), by postulating and analyzing a model of helical buckling pattern of fiber segments with the interior of the embedding cell ellipsoids as an elastic support. The results give a small internal elasticity $k$ less than 200 Pa, and collective compressive forces ranging from a few hundreds of pN to a few $\mu$N generated by U87 ellipsoid aggregates. We also explain that the use of crosslinked gelatin for fiber material (with roughly 100 kPa in Young's modulus) is well-suited in the U87 cell aggregate system, and may also be so for other similar tissue aggregation systems, in order to minimize cell-probe interaction while producing a pronounced buckling pattern, compared with the fiber radius. It is envisaged that by incorporating a fluorescent moiety within the gelatin hydrogel fibers will permit real-time, continuous monitoring of the multi-cellular aggregation mechanics. Future outlook could also include fabricating the probing fibers to exhibit fluorescent, piezoelectric [48], or conductive [49] properties, such that one can monitor the fiber deformation *in situ*. Standardization of the fiber-devices could lay down the potential for a high-throughput platform for biomarker discovery.

## Author's contributions

YYSH. and EMT conceived and supervised the project. C-TL performed the theoretical analysis. ELG performed the experiments unless otherwise stated. WW prepared the experimental figures. MG provided the U87 cell line and performed the immunostaining and confocal microscopy. All authors contributed to writing and reviewing the manuscript.

## Conflict of interest

The authors declare that they have no known competing financial interests or personal relationships that could have appeared to influence the work reported in this paper.

## Acknowledgment

This work was supported by the European Research Council (ERC-StG, 758865) and ELG was a grateful recipient of a WD Armstrong Trust Studentship. WW gratefully acknowledges support from the China Scholarship Council.

## ORCID iDs

Cheng-Tai Lee https://orcid.org/0000-0003-1916-039X
Elisabeth L Gill https://orcid.org/0000-0003-4191-4768
Wenyu Wang https://orcid.org/0000-0001-6580-8236
Eugene M Terentjev https://orcid.org/0000-0003-3517-6578
Yan Yan Shery Huang https://orcid.org/0000-0003-2619-730X

## References

[1] Mehta G, Hsiao A Y, Ingram M, Luker G D and Takayama S 2012 Opportunities and challenges for use of tumor spheroids as models to test drug delivery and efficacy *J. Control. Release* **164** 0168–3659
[2] Langhans S A 2019 Three-dimensional *in vitro* cell culture models in drug discovery and drug repositioning *Front. Pharmacol.* **9** 6
[3] Lin R-Z and Chang H-Y 2008 Recent advances in three-dimensional multicellular spheroid culture for biomedical research *Biotechnol. J.* **3** 1172–84
[4] Achilli T-M, Meyer J and Morgan J R 2012 Advances in the formation, use and understanding of multi-cellular spheroids *Expert Opin. Biol. Ther.* **12** 1347–60
[5] Wells R G 2013 Tissue mechanics and fibrosis *Biochim. Biophys. Acta, Mol. Basis Dis.* **1832** 884–90
[6] Mammoto T, Mammoto A and Ingber D E 2013 Mechanobiology and developmental control *Annu. Rev. Cell Dev. Biol.* **29** 27–61
[7] Vining K H and Mooney D J 2017 Mechanical forces direct stem cell behaviour in development and regeneration *Nat. Rev. Mol. Cell Biol.* **18** 728–42
[8] Fadnes H O, Reed R K and Aukland K 1977 Interstitial fluid pressure in rats measured with a modified wick technique *Microvasc. Res.* **14** 27–36
[9] Boucher Y, Baxter L T and Jain R K 1990 Interstitial pressure gradients in tissue-isolated and subcutaneous tumors: implications for therapy *Cancer Res.* **50** 4478–84
[10] Forgacs G, Foty R A, Shafrir Y and Steinberg M S 1998 Viscoelastic properties of living embryonic tissues: a quantitative study *Biophys. J.* **74** 2227–34
[11] Winters B S, Shepard S R and Foty R A 2005 Biophysical measurement of brain tumor cohesion *Int. J. Cancer* **114** 371–9
[12] Guevorkian K, Colbert M J, Durth M, Dufour S and Brochard-Wyart F 2010 Aspiration of biological viscoelastic drops *Phys. Rev. Lett.* **104** 218101
[13] Campàs O *et al* 2014 Quantifying cell-generated mechanical forces within living embryonic tissues *Nat. Methods* **11** 183–9
[14] Dolega M E, Delarue M, Ingremeau F, Prost J, Delon A and Cappello G 2017 Cell-like pressure sensors reveal increase of mechanical stress towards the core of multicellular spheroids under compression *Nat. Commun.* **8** 14056
[15] Blumlein A, Williams N and McManus J 2017 The mechanical properties of individual cell spheroids *Sci. Rep.* **7** 7346
[16] Mark C *et al* 2020 Correction: collective forces of tumor spheroids in three-dimensional biopolymer networks *eLife* **9** e51912
[17] Gill E L, Willis S, Gerigk M, Cohen P, Zhang D, Li X and Huang Y Y S 2019 Fabrication of designable and suspended microfibers via low-voltage 3D micropatterning *ACS Appl. Mater. Interfaces* **11** 19679–90
[18] Gill E L, Wang W, Liu R and Huang Y Y S 2020 Additive batch electrospinning patterning of tethered gelatin hydrogel fibres with swelling-induced fibre curling *Addit. Manuf.* **36** 101456
[19] Li Z *et al* 2018 Solution fibre spinning technique for the fabrication of tuneable decellularised matrix-laden fibres and fibrous micromembranes *Acta Biomater.* **78** 111–22
[20] Buxboim A, Ivanovska I L and Discher D E 2010 Matrix elasticity, cytoskeletal forces and physics of the nucleus: how deeply do cells 'feel' outside and in? *J. Cell Sci.* **123** 297–308
[21] Timoshenko S and Gere J M 1961 *Theory of Elastic Stability* (New York: McGraw-Hill)
[22] Oldfather W A, Ellis C A and Brown D M 1933 Leonhard Euler's elastic curves *Isis* **20** 72–160
[23] Domokos G, Holmes P and Royce B 1997 Constrained Euler buckling *J. Nonlinear Sci.* **7** 281–314
[24] Goriely A, Vandiver R and Destrade M 2008 Nonlinear Euler buckling *Proc. R. Soc.* A **464** 3003–19
[25] Lee N-K, Johner A and Hong S-C 2007 Compressing a rigid filament: buckling and cyclization *Eur. Phys. J.* E **24** 229–41
[26] Antman S S 2005 *Nonlinear Problems of Elasticity* (Heidelberg: Springer)
[27] Winkler E 1867 *Die Lehre von der Elasticitaet und Festigkeit mit besondere Ruecksicht auf ihre Anwendung in der Technik, fuer polytechnische Schuhlen, Bauakademien, Ingenieure, Maschienenbauer, Architecten, etc.* (Prague: H. Dominicius)
[28] Brangwynne C P, MacKintosh F C, Kumar S, Geisse N A, Talbot J, Mahadevan L, Parker K K, Ingber D E and Weitz D A 2006 Microtubules can bear enhanced compressive loads in living cells because of lateral reinforcement *J. Cell Biol.* **173** 733–41
[29] Dillard D A, Mukherjee B, Karnal P, Batra R C and Frechette J 2018 A review of Winkler's foundation and its profound influence on adhesion and soft matter applications *Soft Matter* **14** 3669–83

[30] Lee C-T and Terentjev E M 2018 Microtubule buckling in an elastic matrix with quenched disorder *J. Chem. Phys.* **149** 145101
[31] Chen Y, Liu Y, Yan Y, Zhu Y and Chen X 2016 Helical coil buckling mechanism for a stiff nanowire on an elastomeric substrate *J. Mech. Phys. Solids* **95** 25–43
[32] Chen Y, Liao X, Liu Y and Chen X 2017 Helical buckling of wires embedded in a soft matrix under axial compression *Extreme Mech. Lett.* **17** 71–6
[33] Deck J H N, Eng L F, Bigbee J and Woodcock S M 1978 The role of glial fibrillary acidic protein in the diagnosis of central nervous system tumors *Acta Neuropathol.* **42** 183–90
[34] Duffy P E, Huang Y-Y, Rapport M M and Graf L 1980 Glial fibrillary acidic protein in giant cell tumors of brain and other gliomas *Acta Neuropathol.* **52** 51–7
[35] Duffy P E, Huang Y-Y and Rapport M M 1982 The relationship of glial fibrillary acidic protein to the shape, motility, and differentiation of human astrocytoma cells *Exp. Cell Res.* **139** 145–57
[36] Peraud A, Mondal S, Hawkins C, Mastronardi M, Bailey K and Rutka J T 2003 Expression of fascin, an actin-bundling protein, in astrocytomas of varying grades *Brain Tumor Pathol.* **20** 53–8
[37] Restrepo A, Smith C A, Agnihotri S, Shekarforoush M, Kongkham P N, Seol H J, Northcott P and Rutka J T 2011 Epigenetic regulation of glial fibrillary acidic protein by DNA methylation in human malignant gliomas *Neuro-Oncology* **13** 42–50
[38] Yu M, Mahtabfar A, Beelen P, Demiryurek Y, Shreiber D I, Zahn J D, Foty R A, Liu L and Lin H 2018 Coherent timescales and mechanical structure of multicellular aggregates *Biophys. J.* **114** 2703–16
[39] Discher D E, Mooney D J and Zandstra P W 2009 Growth factors, matrices, and forces combine and control stem cells *Science* **324** 1673–7
[40] Arda K, Ciledag N, Aktas E, Arıbas B K and Köse K 2011 Quantitative assessment of normal soft-tissue elasticity using shear-wave ultrasound Elastography *Am. J. Roentgenol.* **197** 532–6
[41] Huang G, Wang L, Wang S, Han Y, Wu J, Zhang Q, Xu F and Lu T J 2012 Engineering three-dimensional cell mechanical microenvironment with hydrogels *Biofabrication* **4** 042001
[42] Achterberg V F, Buscemi L, Diekmann H, Smith-Clerc J, Schwengler H, Meister J-J, Wenck H, Gallinat S and Hinz B 2014 The nano-scale mechanical properties of the extra-cellular matrix regulate dermal fibroblast function *J. Invest. Dermatol.* **134** 1862–72
[43] Liu J, Zheng H, Poh P, Machens H-G and Schilling A 2015 Hydrogels for engineering of perfusable vascular networks *Int. J. Mol. Sci.* **16** 15997–6016
[44] Maskarinec S A, Franck C, Tirrell D A and Ravichandran G 2009 Quantifying cellular traction forces in three dimensions *Proc. Natl Acad. Sci.* **106** 22108–13
[45] Trichet L, Le Digabel J, Hawkins R J, Vedula S R K, Gupta M, Ribrault C, Hersen P, Voituriez R and Ladoux B 2012 Evidence of a large-scale mechanosensing mechanism for cellular adaptation to substrate stiffness *Proc. Natl Acad. Sci.* **109** 6933–8
[46] Rape A D, Guo W-h and Wang Y-l 2011 The regulation of traction force in relation to cell shape and focal adhesions *Biomaterials* **32** 2043–51
[47] Tinevez J-Y, Schulze U, Salbreux G, Roensch J, Joanny J-F and Paluch E 2009 Role of cortical tension in bleb growth *Proc. Natl Acad. Sci.* **106** 18581–6
[48] Wang W, Stipp P N, Ouaras K, Fathi S and Huang Y Y S 2020 Broad bandwidth, self-powered acoustic sensor created by dynamic near-field electrospinning of suspended, transparent piezoelectric nanofiber mesh *Small* **16** 2000581
[49] Wang W, Ouaras K, Rutz A L, Li X, Gerigk M, Naegele T E, Malliaras G G and Huang Y Y S 2020 Inflight fiber printing toward array and 3D optoelectronic and sensing architectures *Sci. Adv.* **6** eaba0931